Dynamics of Aero-Engine Dual-Rotor Systems under Multi-Flight Attitudes and Simultaneous Rub-Impact Faults

Peixun Tang[1,2] – Zhengminqing Li[1,2] ✉ – Xiaojing Ma[1,2] – Yiyan Chen[1,2] – Xi Liu[1,2]

[1] College of Mechanical and Electrical Engineering, Nanjing University of Aeronautics and Astronautics, Nanjing 210016, China

[2] National Key Laboratory of Helicopter Aeromechanics, Nanjing University of Aeronautics and Astronautics, Nanjing 210016, China

✉ lzmq_cmee@nuaa.edu.cn

Abstract *High-maneuverability combat aircraft exert extreme loads on aero-engines, potentially triggering destructive rotor-stator rub-impacts and thereby pose a severe threat to flight safety. This study establishes a four-degree-of-freedom (4-DOF) rotor-bearing-disk model for a dual-disk system, specifically tailored to simulate the coupling effects of simultaneous rub-impact faults under diverse flight attitudes and maneuver loads. For benchmarking purposes, a corresponding model free of rub-impact is accordingly constructed. The Newmark-β method is employed to derive solutions for both models. To evaluate how maneuver loads influence the dynamic characteristics of the system, a parametric investigation is conducted to assess the effects of dual-disk rub-impact across three key flight attitudes, namely, rolling, pitching, and yawing. This research offers a critical theoretical basis for enhancing vibration control and conducting failure analysis in fighter engine design, ultimately contributing to the development of safer and more reliable rotor systems.*

Keywords *rotor dynamics, maneuvering flight, bearing nonlinear force, rub-impact, nonlinear characteristic*

Highlights

- *Dual-disk rub-faults show higher vibration and richer spectra under all flight conditions.*
- *Pitching (G = 2.5–7.5) causes peak vibration; yawing dominates X-direction response.*
- *Spectrogram at G = 2.5 shows the richest spectral features across loading conditions and*
- *Bifurcation diagrams show frequent regime shifts under pitching at G = 2 with rub-impact.*

1 INTRODUCTION

The continuous advancement of various technologies has significantly enhanced the maneuverability of modern fighter aircraft, enabling them to execute complex tactical maneuvers and gain air supremacy. Aircraft maneuverability refers to the capability of an aircraft to alter its flight energy, direction, spatial position, and orientation relative to the airframe. It is commonly quantified using specific maneuverability metrics [1].

In recent years, numerous researchers have investigated rotor system dynamics under flight conditions. Sakata et al. [2,3] studied a flexible rotor system with a movable base, analyzed its behavior under pitching motion and demonstrated a good agreement between theoretical and experimental results. Wei and Fan [4] developed a dynamic model for a dual-rotor system using the transfer matrix method and derived expressions for additional loads during composite maneuvers such as horizontal circling, diving, and pull-up. Zhu and Chen [5] established the equations of motion for a multi-disk rotor system under arbitrary flight attitudes applying Lagrange's equations. Hou and Chen [6] investigated the dynamic behavior of a nonlinear aircraft rotor system during Herbst maneuvering flight, with emphasis on load control for safety considerations. The equations of motion were established using Lagrange's equations, incorporating flight parameters to characterize the influence of maneuvering flight. Han and Chu [7] as well as Chen et al. [8], examined subharmonic and mixed resonance in a cracked rotor under foundation excitation, accounting for the angular motion of the aircraft. Gao et al. [9] created a simplified aero-engine rotor model and employed finite element analysis to assess how maneuvering loads affect blade tip clearance. Pan et al. [10] developed a model of a rotor-bearing-disk system to analyze dynamic responses under rolling, pitching, and yawing loads, noting that different flight modes could lead to distinct rub-impact and frequency separation phenomena. Friction faults have consistently been a major concern for researchers, as they are one of the primary causes of vibration in fighter engines. Saeed et al. [11] examined the oscillatory properties of a controlled asymmetric rotor system during rotor-stator rub-impact events and developed the governing equations for the system's dynamics, which incorporate both rub and impact forces. Wu et al. [12] established a nonlinear dynamic model of a dual-rotor-support-casing system. They refined the casing modeling using the finite element method (FEM) and component mode synthesis (CMS), treating inter-shaft rub-impact as a nonlinear excitation, and investigated the effects of rub stiffness and rotational speed ratio on self-excited vibration. Prabith and Krishna [13] employed a time-variational method to study the rub-impact stability of a dual-rotor system under co-rotation and counter-rotation conditions, evaluating the influence of key parameters such as contact stiffness, friction coefficient, and clearance. Pan et al. [14] developed a comprehensive finite element model of a rotor system that integrates multiple nonlinear factors, including blade-casing rub-impact forces, climbing maneuver loads, nonlinear Hertzian contact in bearings, rotor unbalance, gravity, and squeeze film damper effects. They systematically evaluated the dynamic response of the system under varying rub-impact stiffness values, oil film clearances, and bearing clearances. Lin et al. [15] investigated blade-coating rub-impact defects in aero-engines by developing a finite element model validated through a rotor test-rig and a coupled rotor-blade-coating system with a 0-2-1 support configuration. They identified the key

DOI: 10.5545/sv-jme.2025.1428

vibration response characteristics through quantitatively analyzing rub-impact forces at different rotational speeds and invasion depths. Sousa et al. [16] developed a dynamic model of a disk-shaft-bearing system based on Lagrange's equations and the finite element method, which incorporates the strain energy and kinetic energy of the shaft, as well as the kinetic energies of the disk and unbalance mass. Their work has provided a comprehensive theoretical and experimental investigation of the dynamic behavior of rotating machinery under the combined effects of base excitation and disk-stator rub-impact. Yu et al. [17,18] developed a modal analysis method for aero-engine rotors under friction and investigated the complex nonlinear modes of a hybrid rotor system and their effects on vibration responses.

Rotor systems, both in aero-engines and other applications, have been extensively studied worldwide. Prior research has examined the influence of maneuvering loads on aero-engine rotor systems, providing valuable theoretical insights into their behavior under various flight conditions. Several studies have developed rotor system models that incorporate multiple nonlinear components, enabling more comprehensive analyses. Others have integrated rub-impact faults into rotor dynamics modeling, laying a foundation for investigating failure mechanisms. Nonetheless, studies on dual-disc aero-engine rotor systems experiencing simultaneous rub-impact under multi-directional maneuvering loads remain limited. To address this gap, it is essential to develop a dynamic analysis model capable of simulating rub-impact defects and multi-directional maneuver loads. This study makes the following specific contributions: (1) Conduct a systematic investigation into the dynamics of the rotor under three fundamental flight attitudes: rolling, pitching, and yawing; (2) Develop a nonlinear dynamic model that integrates rub-impact force (for dual-disks), gravity, disk unbalance force, maneuver load-induced excitations, and nonlinear bearing force, and solve it using a Newmark-β numerical scheme tailored for complex rotor systems; (3) Perform a comparative analysis of the rotor system's response with and without dual-disk rub-impact faults across various flight attitudes, and a comparative analysis of dynamic responses across multiple flight conditions under the coupling of rub-impact and varying flight attitudes (different load conditions).

2 METHODS AND MATERIALS

2.1 System Assumptions and Total Degrees of Freedom

In practice, the rotor system of a traditional aero-engine exhibits high complexity due to the presence of multiple components and intricate interactions. In this research, the system is reduced to a two-disc rotor bearing system, with the remaining essential assumptions listed below:

1. Modern fighter aircraft are typically equipped with 1 to 3 engines, and for the sake of this study, the rotor system of the fighter engine is assumed to be situated at the fighter's center of mass.
2. The entire aero-engine rotor system has been streamlined into a single flexible shaft with two centered mass disks.
3. Rotor unbalance is assumed to occur on a single plane, as this represents a common and critical source of vibration in practical rotor systems.
4. The model's central axis is elastic, with torsional and axial vibrations of the spinning axis neglected.

The finite element approach is used to create a rotor-bearing system model with 5 nodes and 24 degrees of freedom based on the assumptions listed above. Out of these 24 degrees of freedom, 20 are the total degrees of freedom of the 5 nodes, with the remaining 4 being the degrees of freedom of the 2 supporting bearing outer rings in the X and Y axes.

2.2 Basis of Finite Element Theory

The Rayleigh model is used primarily in this research to develop the finite element model design of the rotor-rolling bearing's shaft of part. Each node of the Rayleigh beam has 4 degrees of freedom, as illustrated in Fig. 1, and the generalized coordinate system is stated as:

$$\mathbf{u}=\left[x_a,y_a,\theta_{xa},\theta_{ya},x_b,y_b,\theta_{xb},\theta_{yb}\right]^T \tag{1}$$

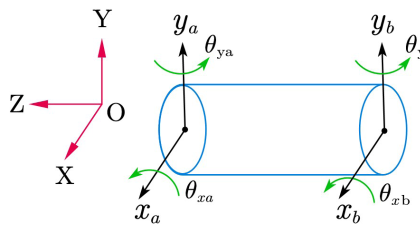

Fig. 1. Finite element model of rotor shaft (Rayleigh beam model)

The Rayleigh beam element model's mass, stiffness, damping, and gyroscopic moment matrix can all been solved using the Lagrange's equation and numerical programming tools [19]. The particular matrices are given in Eqs. (2) to (5):

$$\mathbf{M}_s^T=\frac{\rho\pi\left(R^2-r^2\right)l}{420}\begin{bmatrix}156&0&0&22l&54&0&0&-13l\\0&156&-22l&0&0&54&13l&0\\0&-22l&4l^2&0&0&-13l&-3l^2&0\\22l&0&0&4l^2&13l&0&0&-3l^2\\54&0&0&13l&156&0&0&-22l\\0&54&-13l&0&0&156&22l&0\\0&13l&-3l^2&0&0&22l&4l^2&0\\-13l&0&0&-3l^2&-22l&0&0&4l^2\end{bmatrix}, \tag{2}$$

$$\mathbf{M}_s^R=\frac{\rho\pi\left(R^4-r^4\right)}{120l}\begin{bmatrix}36&0&0&3l&-36&0&0&3l\\0&36&-3l&0&0&-36&-3l&0\\0&-3l&4l^2&0&0&3l&-l^2&0\\3l&0&0&4l^2&-3l&0&0&-l^2\\-36&0&0&-3l&36&0&0&-3l\\0&-36&3l&0&0&36&3l&0\\0&-3l&-l^2&0&0&3l&4l^2&0\\3l&0&0&-l^2&-3l&0&0&4l^2\end{bmatrix}, \tag{3}$$

$$\mathbf{K}_s=\frac{E\pi\left(R^4-r^4\right)}{4l^3}\begin{bmatrix}12&0&0&6l&-12&0&0&6l\\0&12&-6l&0&0&-12&-6l&0\\0&-6l&4l^2&0&0&6l&2l^2&0\\6l&0&0&4l^2&-6l&0&0&2l^2\\-12&0&0&-6l&12&0&0&-6l\\0&-12&6l&0&0&12&6l&0\\0&-6l&2l^2&0&0&6l&4l^2&0\\6l&0&0&2l^2&-6l&0&0&4l^2\end{bmatrix}, \tag{4}$$

$$\mathbf{G}_s=\frac{\rho\pi\left(R^4-r^4\right)}{60l}\begin{bmatrix}0&-36&3l&0&0&36&3l&0\\36&0&0&3l&-36&0&0&3l\\-3l&0&0&4l^2&-3l&0&0&-l^2\\0&-3l&4l^2&0&0&-3l&l^2&0\\0&36&-3l&0&0&36&3l&0\\-36&0&0&-3l&36&0&0&3l\\-3l&0&0&l^2&3l&0&0&4l^2\\0&-3l&-l^2&0&0&3l&4l^2&0\end{bmatrix}, \tag{5}$$

2.3 Rolling Bearing Model

Bearings play a critical role as support structures in rotor systems, and the nonlinear contact force influences the rotor system's dynamic behavior. Fig. 2 shows a schematic representation of a rolling bearing, which consists of four main components: an inner ring, an outer ring, rolling elements (balls) and a cage. Additionally, two assumptions must be made while calculating the rolling bearing model:

1. Assume that the ball is evenly placed between the inner and outer ring raceways, and that the ball and raceway are inpure rolling.
2. Assume that the bearing's inner ring is solidly linked to the rotating shaft.

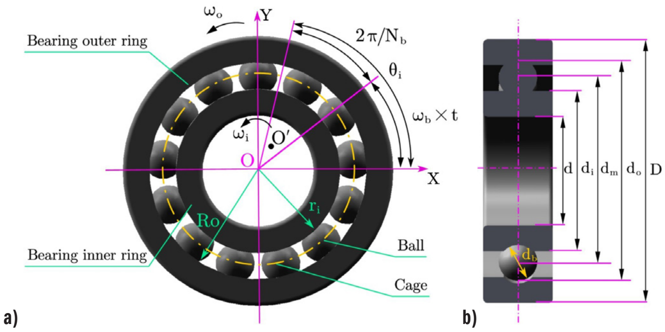

Fig. 2. The diagram of rolling bearing model; a) front view of rolling bearing, b) rolling bearing profile

The outside raceway's radius is denoted as R_o, whereas the inner raceway's radius is r_i, d_i and d_o are the diameters of the bearing's inner and outer rings, respectively, and D is the outer ring diameter of the bearing. The bearing pitching diameter is denoted by d_m, which is equal to: $d_m=(d_i+d_o)/2$, [20].

Assume that the linear speed of the contact point between a ball and the bearing outer ring is v_o, the linear speed of the contact point with the bearing inner ring is v_i, the rotational speed of the bearing outer ring is ω_o, the rotation angular speed of the inner ring is ω_i, and the radius of the outer raceway is R_o. The inner raceway radius is r_i. So v_i and v_o can be represented as:

$$v_i=\omega_i r_i, \quad v_o=\omega_o R_o, \tag{6}$$

Given that the bearing's outer ring is stationary, the formula for calculating the cage speed is as follows:

$$v_c=(v_i+v_o)/2\,. \tag{7}$$

The angular velocity of the bearing cage is further derived as:

$$\omega_c=\frac{\omega_i r_i}{R_o+r_i}, , \tag{8}$$

Given the number of bearing balls is N_b and the angular position of the j ball is θ_j, then:

$$\theta_j=\omega_c t+\frac{2\pi}{N_b}(j-1), \quad j=1,2,3,\cdots,N_b\,. \tag{9}$$

The Hertz contact theory states that if the normal contact deformation δ_{bj} between the ball and the raceway is positive, the contact pressure between them is given by the f_{bj} as:

$$f_{bj}=K_b(\delta_{bj})^{3/2}=K_b\left(x\cos\theta_{bj}+y\sin\theta_{bj}-\delta_0\right)^{3/2} \cdot H(x\cos\theta_{bj}+y\sin\theta_{bj}-\delta_0). \tag{10}$$

In Equation (10), K_b represents the Hertz contact stiffness, the value of δ_0 is the bearing clearance, contact variable is $\delta_j=x\cos\theta_j+y\sin\theta_j-\delta_0$, and $H(\delta_j)$ the Heaviside function:

$$H(\delta_j)=\begin{cases}1, & H(\delta_j)>0\\ 0, & H(\delta_j)<0\end{cases}.$$

Therefore, the bearing force in the X and Y directions can be described as follows using the Hertz contact theory mentioned above:

$$\begin{cases}F_{b_x}=\sum_{j=1}^{N_b} f_{jx}\\ F_{b_y}=\sum_{j=1}^{N_b} f_{jy}\end{cases}. \tag{11}$$

2.4 Rub-Impact Force Model

Figure 3 depicts the mechanical model of rotor rub-impact, where O is the position of the rotor center of mass at rest. When the rotor's displacement r exceeds the clearance δ_c between the rotor and stator, rub-impact occurs. The rotor's displacement r is defined $r=\sqrt{x^2+y^2}$ [21].

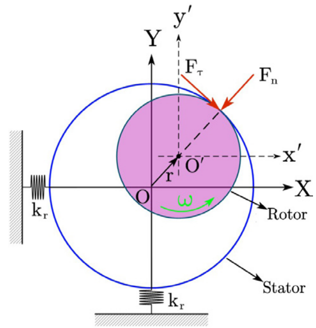

Fig. 3. Schematic representation of the rub-impact phenomenon between the stator and rotor

In addition, K_o indicates rub-impact stiffness, F_n represents normal force, F_τ is determined by Coulomb's law, which is tangential force, and μ represents friction coefficient. The normal and tangential forces during rub-impact are calculated as follows:

$$\begin{cases}F_n=\begin{cases}0 & \text{if } r\le\delta\\ k_o(r-\delta) & \text{if } r>\delta\end{cases},\\ F_\tau=\mu\cdot F_n\end{cases} \tag{12}$$

The rub-impact force can be decomposed into Cartesian coordinates xoy,

$$\begin{bmatrix}f_y\\ f_x\end{bmatrix}=-K\frac{k_o(r-\delta)}{r}\begin{bmatrix}1 & -\mu\\ \mu & 1\end{bmatrix}\begin{bmatrix}x\\ y\end{bmatrix}, \tag{13}$$

where K is the Heaviside function, and the contact angle is $\gamma=\arctan\left(y/x\right)$. When $r>\delta$, $K=1$, otherwise, $K=0$.

2.5 Modeling of 3 Basic Flight Attitudes (Rolling, Pitching, Yawing)

The work of Zhu and Chen [5] established the foundation for the maneuvering flight model, detailing its derivation and results. Based on the assumptions outlined in Section 2.1, the basic coordinates of the aircraft engine in flight are given, and the fighter is defined as pitching flight by twisting around the X axis, rolling flight around the Z axis and yawing flight around the Y axis, which are described in Fig. 4. Based on the Hamiltonian principle, the kinetic and potential energy of the rotor support system, as well as the Lagrange function are computed, and the differential equation for the system's motion is derived. The matrix of increased damping $\mathbf{C}_{\mathrm{B,i}}$, stiffness $\mathbf{K}_{\mathrm{B,i}}$, and load introduced by maneuvering flight $\mathbf{F}_{\mathrm{B,i}}$ is shown below:

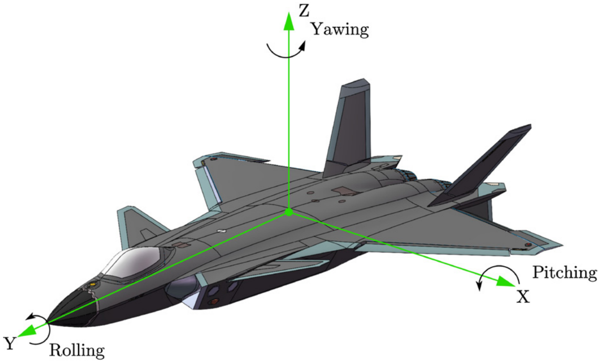

Fig. 4. Schematic diagram of the 3 basic flight attitudes of a fighter aircraft

$$\mathbf{K}_{\mathrm{B,i}} = \begin{bmatrix} -m_i\left(\dot{\theta}_{B,y}^2+\dot{\theta}_{B,z}^2\right) & m_i\left(\dot{\theta}_{B,x}\dot{\theta}_{B,y}-\dot{\theta}_{B,z}\right) & 0 & 0 \\ m_i\left(\dot{\theta}_{B,x}\dot{\theta}_{B,y}-\dot{\theta}_{B,z}\right) & -m_i\left(\dot{\theta}_{B,x}^2+\theta_{B,z}^2\right) & 0 & 0 \\ 0 & 0 & 0 & 0 \\ 0 & 0 & 0 & 0 \end{bmatrix}, \quad (14)$$

$$\mathbf{C}_{\mathrm{B,i}} = \begin{bmatrix} 0 & -2m_i\dot{\theta}_{B,z} & 0 & 0 \\ 2m_i\dot{\theta}_{B,z} & 0 & 0 & 0 \\ 0 & 0 & 0 & 0 \\ 0 & 0 & 0 & 0 \end{bmatrix}, \quad (15)$$

$$\mathbf{F}_{\mathrm{B,i}} = \begin{bmatrix} -m_i\left(\dot{X}_B-\dot{\theta}_{B,z}Y_B+\dot{\theta}_{B,y}\dot{Z}_B\right)-m_iz_i\left(\dot{\theta}_{B,x}\dot{\theta}_{B,z}+\ddot{\theta}_{B,y}\right) \\ -m_i\left(\ddot{Y}_B-\dot{\theta}_{B,z}X_B+\dot{\theta}_{B,x}\dot{Z}_B\right)-m_iz_i\left(\dot{\theta}_{B,y}\dot{\theta}_{B,z}+\ddot{\theta}_{B,x}\right) \\ -I_i\ddot{\theta}_{B,x}-\Omega I_{p,i}\dot{\theta}_{B,y} \\ \Omega I_{p,i}\dot{\theta}_{B,x}-I_i\ddot{\theta}_{B,y} \end{bmatrix}, \quad (16)$$

In Equations (14) to (16) $\ddot{X}_B, \ddot{Y}_B$, and $\ddot{Z}_B$ denote the linear accelerations along the X, Y, and Z axes, respectively, while $\ddot{\theta}_{B,x}, \ddot{\theta}_{B,y}$, and $\ddot{\theta}_{B,z}$ represent the angular accelerations about these axes. Similarly, $\dot{X}_B, \dot{Y}_B$, and $\dot{Z}_B$ refer to the corresponding linear velocities, and $\dot{\theta}_{B,x}, \dot{\theta}_{B,y}$, and $\dot{\theta}_{B,z}$ indicate the angular velocities about the X, Y, and Z axes.

2.6 Global Equation of Aero-Engine Rotor Dynamics

Building on the theoretical descriptions of the components of the rotor subsystem provided in Sections 2.1 to 2.5, this section describes the assembly of the complete rotor system, with its three-dimensional structure shown in Fig. 5. Furthermore, when paired with the fundamental equation of rotor dynamics, the overall motion equation of rotor dynamics under multi-factor conditions is completed, as presented in Eq. (17). It should be mentioned that Pan et al. [10] demonstrated the correctness of the dynamic modeling approach in the study and validated that the modeling method is not impacted by the number of nodes or whether is a step axis. $\mathbf{M}_{\mathrm{all}}$ indicates the mass matrix of the entire system, and $\mathbf{C}_{\mathrm{all}}$ represents the damping matrix of the entire system, $\mathbf{K}_{\mathrm{all}}$ covers the stiffness matrix of the whole system, $\mathbf{G}_{\mathrm{all}}$ represents the gyro matrix of the total system, and $\mathbf{C}_B$ and $\mathbf{K}_B$ represent the additional damping matrix and stiffness matrix created by maneuvering loads, respectively.

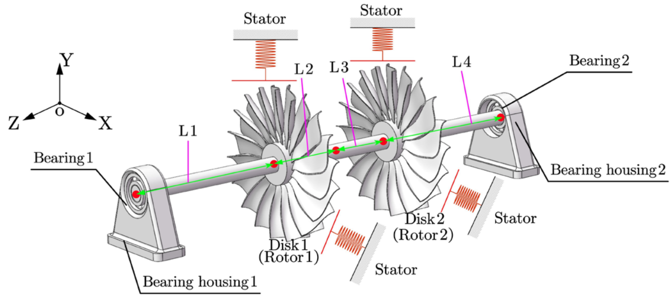

Fig. 5. Schematic of the entire rotor system

$\mathbf{F}_e$ represents the imbalance force matrix of the disc, $\mathbf{F}_b$ represents the bearing's nonlinear force matrix, $\mathbf{F}_a$ represents the dynamic load force matrix, $\mathbf{F}_g$ signifies the gravity matrix, and $\mathbf{F}_{\mathrm{rub}}$ illustrates the disk's rub-impact force matrix.

$$\mathbf{M}_{\mathrm{all}}\ddot{\mathbf{X}}+\left(\mathbf{C}_{\mathrm{all}}-\omega\mathbf{G}_{\mathrm{all}}+\mathbf{C}_B\right)\dot{\mathbf{X}}+\left(\mathbf{K}_{\mathrm{all}}+\mathbf{K}_B\right)\mathbf{X} = \mathbf{F}_e+\mathbf{F}_b+\mathbf{F}_a+\mathbf{F}_g+\mathbf{F}_{\mathrm{rub}}. \quad (17)$$

The mass of rotor system is expressed as follows. $\mathbf{M}_{\mathrm{all}}$ contains the mass matrix of the shaft, disks, and bearing outer rings. The two support bearings' outer rings possess centralized masses of m_{b1} and m_{b2}, respectively.

$$\mathbf{M}_{\mathrm{all}} = \begin{bmatrix} \mathbf{M} & & & & \\ & m_{b1} & & & \\ & & m_{b1} & & \\ & & & m_{b2} & \\ & & & & m_{b2} \end{bmatrix}.. \quad (18)$$

The damping of rotor system is expressed as follows: $\mathbf{C}$ is the proportional damping matrix of the shaft, specifically Rayleigh damping as used in this paper, calculated via Eq. (19). Here, $\alpha=2(\xi_1/\omega_1-\xi_2/\omega_1)/(1/\omega_2^2-\omega_1^2)$ and $\beta=2(\xi_2\omega_2-\xi_1\omega_1)/(\omega_2^2-\omega_1^2)$ where ξ_1, ξ_2 and ω_1, ω_2 denote the rotor system's first two damping ratios and natural frequencies, while c_{b1} and c_{b2} represent the connection damping between the bearing's supporting outer ring and bearing housing.

$$\mathbf{C} = \alpha\mathbf{M}+\beta\mathbf{K}, \quad (19)$$

$$\mathbf{C}_{\mathrm{all}} = \begin{bmatrix} \mathbf{C} & & & & \\ & c_{b1} & & & \\ & & c_{b1} & & \\ & & & c_{b2} & \\ & & & & c_{b2} \end{bmatrix}. \quad (20)$$

The gyro matrix of the rotor system is composed as follows:

$$\mathbf{G}_{\mathrm{all}} = \begin{bmatrix} \mathbf{G} & & & & \\ & 0 & & & \\ & & 0 & & \\ & & & 0 & \\ & & & & 0 \end{bmatrix}, \quad (21)$$

where $\mathbf{G}$ represents the matrix of the shaft system and the disc system.

$$\mathbf{K}_{\mathrm{all}} = \begin{bmatrix} \mathbf{K} & & & & \\ & k_{b1} & & & \\ & & k_{b1} & & \\ & & & k_{b2} & \\ & & & & k_{b2} \end{bmatrix}, \quad (22)$$

where $\mathbf{K}$ is the stiffness matrix of the whole shafting. k_{b1} and k_{b2} are bearing1 and bearing2 support stiffness. The extra stiffness, damping, and force matrix of the rotor system under maneuvering load are computed using Eqs. (14) to (16).

$$\mathbf{C}_{\mathrm{B}}=\begin{bmatrix} 0 & -2m_j\omega_z & 0 & 0 \\ 2m_j\omega_z & 0 & 0 & 0 \\ 0 & 0 & 0 & 0 \\ 0 & 0 & 0 & 0 \end{bmatrix}, \quad (j=1,2), \tag{23}$$

$$\mathbf{K}_{\mathrm{B}}=\begin{bmatrix} -m_j\left(\omega_y^2+\omega_z^2\right) & m_j\left(\omega_x\omega_y-\omega_z\right) & 0 & 0 \\ m_j\left(\omega_x\omega_y+\omega_z\right) & -m_j\left(\omega_x^2+\omega_z^2\right) & 0 & 0 \\ 0 & 0 & 0 & 0 \\ 0 & 0 & 0 & 0 \end{bmatrix}, \quad (j=1,2). \tag{24}$$

When the fighter rolling, the additional force is given as:

$$\mathbf{F}_{\mathrm{a}}=\begin{bmatrix} 0,0,0,0,2m_1\omega_x v_z,2m_1\omega_x v_y,0,0,0, \\ 0,0,0,2m_2\omega_x v_z,2m_2\omega_x v_y,0,0,0,0, \\ 2m_{b1}\omega_x v_z,2m_{b1}\omega_x v_y,2m_{b2}\omega_x v_z,2m_{b2}\omega_x v_y \end{bmatrix}^T. \tag{25}$$

When the fighter pitching, the additional force is given as:

$$\mathbf{F}_{\mathrm{a}}=\begin{bmatrix} 0,0,0,0,\pm m_1\omega_x v,0,\pm J_{p1}\omega\omega_x,0,0,0,0, \\ 0,\pm m_2\omega_x v,0,\pm J_{p2}\omega\omega_x,0,0,0,0, \\ 0,\pm m_{b1}\omega_x v,0,\pm m_{b2}\omega_x v,0 \end{bmatrix}^T, \tag{26}$$

where the sign of the force depends on the direction of the pitching motion: a negative sign "–"is used for diving (nose-down motion), and a positive sign "+" is used for climbing (nose-up motion).

When the fighter is undergoing yawing, the additional force induced by the maneuver load is given by:

$$\mathbf{F}_{\mathrm{a}}=\begin{bmatrix} 0,0,0,0,0,m_1\omega_y v,0,J_{p1}\omega\omega_y,0,0,0, \\ 0,0,m_2\omega_y v,0,J_{p2}\omega\omega_y,0,0,0, \\ 0,0,m_{b1}\omega_y v,0,m_{b2}\omega_y v \end{bmatrix}^T. \tag{27}$$

The unbalanced force matrix is:

$$\mathbf{F}_{\mathrm{e}}=\begin{bmatrix} 0,0,0,0,m_1e_1\omega^2\cos(\omega t+\varphi),m_1e_1\omega^2\sin(\omega t+\varphi),0 \\ ,0,0,0,0,0,m_2e_2\omega^2\cos(\omega t+\varphi),m_2e_2\omega^2\sin(\omega t+\varphi), \\ 0,0,0,0,0,0,0,0,0,0,0,0 \end{bmatrix}^T. \tag{28}$$

The gravity matrix is:

$$\mathbf{F}_{\mathrm{g}}=\begin{bmatrix} 0,0,0,0,0,-m_1g,0,0,0,0,0,0,0,0 \\ -m_2g,0,0,0,0,0,0,0,-m_{b1}g,0,-m_{b2}g \end{bmatrix}^T. \tag{29}$$

The bearing nonlinear Hertz force matrix is as follows:

$$\mathbf{F}_{\mathrm{b}}=\begin{bmatrix} -F_{bx1},-F_{by1},0,0,0,0,0,0,0,0,0,0,0,0,0 \\ 0,0,-F_{bx2},-F_{by2},0,0,F_{bx1},F_{by1},F_{bx2},F_{by2} \end{bmatrix}^T. \tag{30}$$

The rub-impact matrix formed between the rotor and stator is:

$$\mathbf{F}_{\mathrm{rub}}=\begin{bmatrix} 0,0,0,0,\ \mathrm{F}_{rubx1},\ \mathrm{F}_{ruby1},0,0,0,0,0,0,0, \\ \mathrm{F}_{rubx2},\ \mathrm{F}_{ruby2},0,0,0,0,0,0,0,0,0,0 \end{bmatrix}^T. \tag{31}$$

The displacement of parameter $\mathbf{X}$ may be written in the form of:

$$\mathbf{X}=\left[\mathbf{x},x_{b1},y_{b1},x_{b2},y_{b2}\right]^T, \tag{32}$$

where $\mathbf{x}$ represents the displacement vector that includes each of the nodes.

3 RESULTS AND DISCUSSION

This section presents a comprehensive analysis of the dynamic behavior of the rotor system under different flight attitudes and maneuver loads. The effects of rub-impact and non-rub-impact conditions on shaft orbits and Y-direction frequency spectra are compared at a rotational speed of ω = 2400 rad/s under maneuvering loads of G = 2.5, G = 5, G = 7.5, and G = 10 (where G denotes the maneuver load intensity, defined as the ratio of the maneuver-induced inertial force to the gravitational force). Additionally, the bifurcation behavior is examined under a fixed maneuvering load of G = 2 within a rotational speed range of 500 rad/s to 3000 rad/s. These analyses are presented in Sections 3.1, 3.2, and 3.3 for pitching, rolling, and yawing maneuver conditions, respectively. Furthermore, Section 3.4 investigates the coupled effects of maneuvering loads and rub-impact under various flight attitudes to assess their influence on the disk 1 subsystem. The same parameter sets as those in Sections 3.1, 3.2, and 3.3 are employed for consistency.

Table 1 lists the key parameters of the rotor system used in the simulations. The calculation formulas for the maneuver load intensity of G under pitching, rolling, and yawing circumstances are as follows: $G=\omega_x v^z/g$, $G=\omega_z v^z/g$ and $G=\omega_y v^z/g$, (g=10 m/s^2).

Table 1. System parameters

Parameter	Symbol	Value
The length of each shaft part [mm]	L_1	180
	L_2	80
	L_3	80
	L_4	180
The mass of disk 1 [kg]	m_1	20
The mass of disk 2 [kg]	m_2	20
The combined mass of support bearing 1 and its outer ring [kg]	m_{b1}, m_{b2}	4, 4
Disk 1 diameter moment of inertia [kg/m^2]	jd_1	3.5×10^{-2}
Disk 2 diameter moment of inertia [kg/m^2]	jd_2	3.5×10^{-2}
Polar moment of inertia of disk 1 [kg/m^2]	jp_1	7×10^{-2}
Polar moment of inertia of disk 2 [kg/m^2]	jp_1	7×10^{-2}
The supporting damping of the bearing 1 and bearing 2 [N·s/m]	c_{b1}, c_{b2}	2×10^3
The supporting stiffness of the bearing 1 and bearing 2 [N/m]	k_{b1}, k_{b2}	2.5×10^7
Elastic modulus of shaft [Pa]	E	2.07×10^{11}
material density [kg/m^3]	ρ	7.85×10^3
Hertz contact stiffness [N/m]	K_b	7×10^9
Number of ball bearings	N_b	13
Clearance between disk and stator [m]	δ	2.5×10^{-5}
Rub-impact stiffness [N/m]	K_o	6.5×10^7
Eccentricity of two lumped mass disks [m]	e_1, e_2	2.5×10^{-5}

3.1 Pitching Maneuver Condition (Rub and Without Rub-Impact)

Figure 6 depicts the axial trajectory map of the disk 1 system under various pitching maneuvering loads, comparing the cases with and without rub-impact. Shaft orbits are a critical tool for analyzing rotor dynamic behavior, as they provide a visual representation of the rotor's lateral motion. Regardless of whether the rub-impact is considered, the system exhibits single-periodic motion, indicating that the maneuver load alone does not induce complex nonlinear motion (e.g., quasi-periodic or chaotic motion) under the tested conditions. In the absence of rub-impact, the overall diagram of shaft orbit changes to the top right corner as the pitching maneuver loads rise, however, vibration displacement in the X and Y axes stays instead similar. In contrast to this conclusion, when the rub-impact is analyzed, the increase in maneuvering load causes disk 1 to increase significantly in the X and Y directions. Nevertheless, the shaft orbit travels to the upper right corner, which is consistent with the no rub-impact case, demonstrating that when subjected to rub-impact, the system's vibration in various directions is magnified, and the vibration displacement in the Y direction is larger.

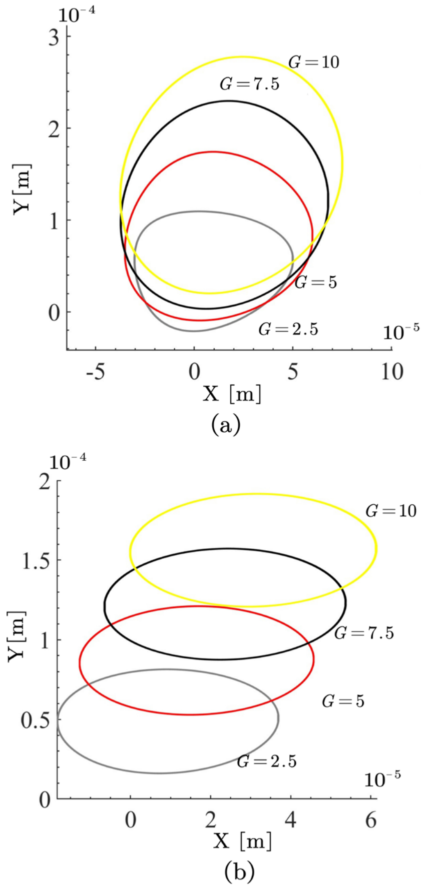

Fig. 6. Shaft orbit diagrams of disk 1 under maneuvering loads in the pitching of aircraft; a) rub impact; b) no rub-impact

Figure 7 displays the results of a fast Fourier transform (FFT) analysis of the vibration of disk 1 (Y direction) under pitching maneuvering loads, revealing significant differences in the frequency spectra between the cases with and without rub-impact. While rub-impact is considered, subharmonic frequency ($0.8f$) and ($0.9f$), and frequency of one-times (f) and two times ($2f$) appear in the spectrum diagram of disc 1, while the one-times frequency and subharmonic frequency ($0.7f$) appear in the spectrum diagram of the disk 1 system with only maneuvering load. In contrast, the one-times frequency of the rub-impact exhibits a greater wave frequency than the no rub-impact. Additionally, as the maneuver load increases, the amplitude of the fundamental frequency increases, which is attributed to the increase in inertial forces that enhance the interaction between the rotor and the stator. Interestingly, as the pitching maneuver load increases, the amplitude of the second harmonic ($2f$) in the spectrogram corresponding to the rub-impact decreases. This phenomenon may be explained by the change in the rub-impact interaction mode: as the load increases, the duration or intensity of the rub-impact may decrease, leading to a reduction in the second harmonic component.

Figure 8 illustrates the Y direction responses of disk 1 under pitching maneuver conditions (G=2), comparing the scenarios with and without rub-impact. In Figure 8a, within the speed range of 500 rad/s to 1300 rad/s, the system undergoes a series of transitions between single-periodic, quasi-periodic, multi-periodic motions. For speeds between 1300 rad/s and 2000 rad/s, the system primarily demonstrates quasi-periodic motion. As the rotational speed further increases, the system undergoes a succession of transitions between single-periodic, multi-periodic and quasi-periodic motions.

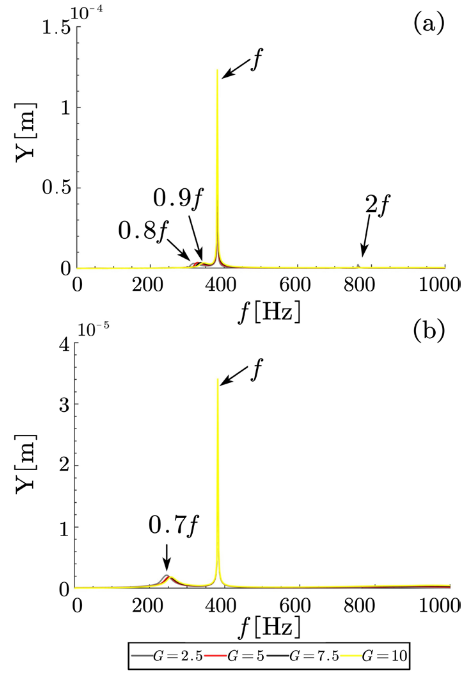

Fig. 7. Disk 1 spectrogram (Y direction) of varied maneuvering loads in the pitching of the aircraft; a) rub-impact, and b) no rub-impact

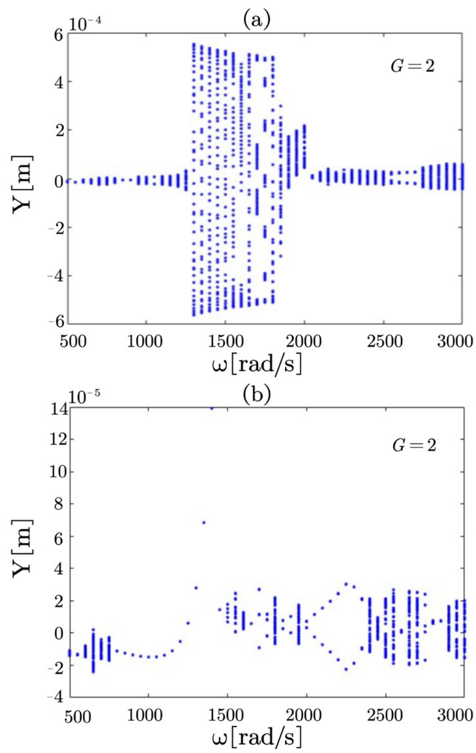

Fig. 8. Bifurcation diagrams of disk 1 in the Y direction under pitching conditions (G = 2); a) rub-impact, and b) no rub-impact

In Figure 8b, between 500 rad/s and 1450 rad/s, the response transitions from quasi-periodic to single-periodic motion. With increasing speed, the system remains quasi-periodic until reaching 1800 rad/s. Within the range of 1800 rad/s to 2350 rad/s, period-doubling bifurcation is observed, and from 2350 rad/s to 3000 rad/s, the motion is predominantly quasi-periodic.

3.2 Rolling Maneuver Condition (Rub and Without Rub-Impact)

Figure 9 depicts the shaft orbits of different loads in a rolling condition. First and foremost, whether or not the influence of rub-impact is addressed, disk 1 mostly exhibits a single period behavior, which is similar to that under pitching maneuvering loads. In the absence of rub-impact, as the rolling load steadily rises, the vibration displacement of each load in the X and Y directions remain relatively constant, but the overall shaft orbit shifts to the bottom right corner. At the same time, it is clear that when the maneuvering load grows, the influence of the rub effect on the X direction displacement increases relative to that absent rub. Furthermore, in the rub-impact diagram, the movement in the X direction expands as the load increases, and the offset path of the shaft orbit motion curve is comparable to that without rub.

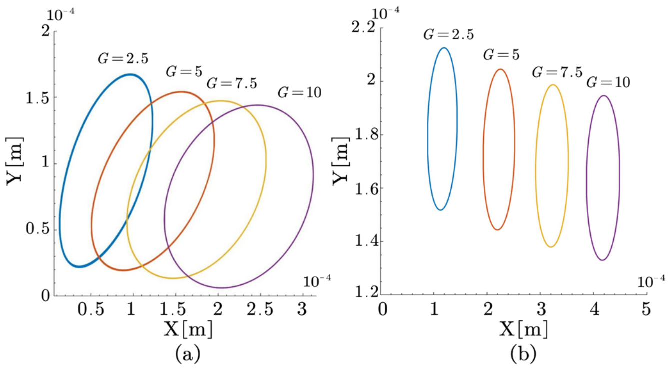

Fig. 9. Shaft orbit diagrams of disk 1 under different maneuvering loads in the rolling of the aircraft; a) rub-impact, and b) no rub-impact

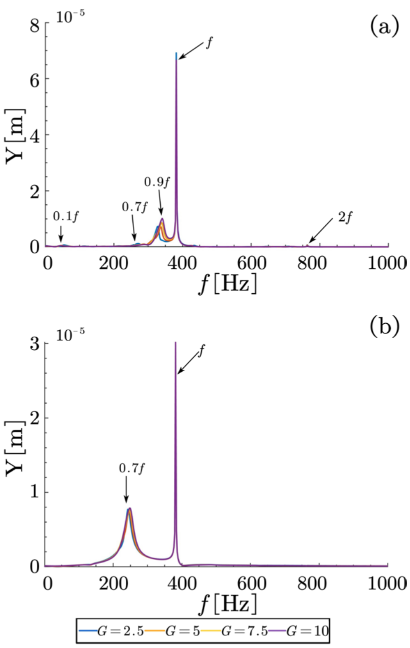

Fig. 10. Disk 1 spectrogram (Y direction) of varied maneuvering loads in the rolling of the aircraft; a) rub-impact, and b) no rub-impact

Figure 10 demonstrates the results of a fast Fourier transform (FFT) examination of rotor vibration under rolling maneuver loads yields considerable spectrum variations (Y direction) with and without rub-impact. When rub-impact is considered, the response of the disk 1 system is composed of the one-times frequency, two-times the frequency, and 3 subharmonic frequencies. It is worth observing that as the load advances, the amplitude of the subharmonic ($0.9f$) increases, but amplitude of the subharmonic ($0.7f$), the amplitudes of the two-times and one-times frequencies drop. In the absence of rub-impact, the disk 1 system's response comprises a one-times frequency and a subharmonic ($0.7f$), with its amplitudes increasing with the load. A comparison of the two figures clearly shows that considering rub-impact introduces additional multiple frequency components and modifies the amplitude distribution of existing frequencies, highlighting the significant influence of rub-impact on the system's frequency characteristics.

Figure 11 illustrates the Y direction responses of disk 1 under rolling maneuver conditions ($G = 2$), comparing scenarios with and without rub-impact. As depicted in sub-figure a, the system exhibits a complex dynamic evolution as the rotational speed increases. Within the speed range of 500 rad/s to 1200 rad/s, the response transitions from single-periodic to quasi-periodic, followed by a multi-periodic bifurcation and further quasi-periodic motion. The motion remains predominantly quasi-periodic from 1200 rad/s to 1900 rad/s. A window of stable single-periodic motion is observed between 1900 rad/s and 2050 rad/s, beyond which the system reverts to quasi-periodic behavior. In contrast, the dynamics presented in sub-figure b is characterized by alternating quasi-periodic and single-periodic motions in the speed range (500 rad/s to 1500 rad/s). As the speed increases, multi-periodic motion becomes dominant, which is a result of the nonlinearity introduced by the bearing forces and maneuver loads. Finally, within the high-speed range of 2400 rad/s to 3000 rad/s, the system undergoes a transition from quasi-periodic to single-periodic motion before returning to a quasi-periodic state.

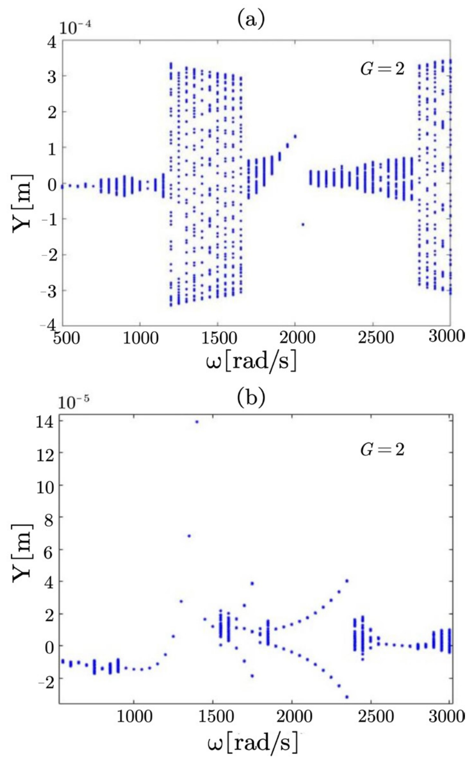

Fig. 11. Bifurcation diagram of disk 1 in the Y direction under rolling conditions (G = 2); a) rub-impact; and b) no rub-impact

3.3 Yawing Maneuver Condition (Rub and Without Rub-Impact)

Figure 12 demonstrates the shaft orbit diagram of disc 1 under yawing attitudes (with various maneuvering loads) with and without the rub-impact. In the absence of the rub-impact, the shaft orbit changes to the upper left as the maneuvering load increases. And the system displays a single period that corresponds to the pitching and rolling findings. Under the influence of rub-impact, as the load increases, the shaft orbit tends to shift to the left, and the vibration displacements in the X and Y directions increase significantly. Moreover, the overall vibration amplitude in the rub-impact case is substantially larger than that in the non-rub-impact case, which is consistent with the observations under pitching and rolling conditions. This consistency indicates that rub-impact has a universal amplifying effect on vibration amplitudes across all three basic flight attitudes.

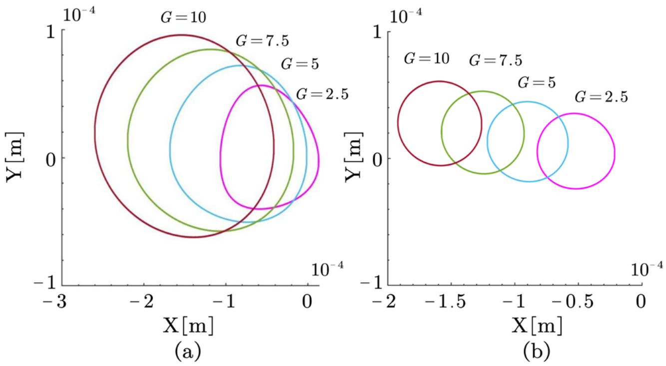

Fig. 12. Shaft orbit diagram of disk 1 under different maneuvering loads in the yawing of the aircraft; a) rub-impact; b) no rub-impact

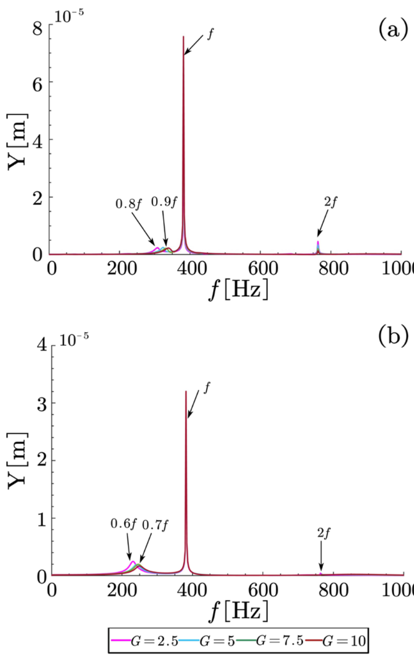

Fig. 13. Spectrogram (Y direction) of disk 1 under different maneuvering loads in the yawing of the aircraft; a) rub-impact; b) no rub-impact

The spectrum diagram (Y direction) of disk 1 with and without the rub-impact is shown in Fig. 13 under yawing flight attitude (various maneuvering loads). In the absence of the rub-impact, the system produces 2 subharmonic frequencies, a two-times frequency and a one-times frequency, which is more comparable to the output when the rub is present. However, it is evident that the amplitudes of one-times and two times frequency when the influence of the rub is taken into account is greater than when it is not. In the non-rub-impact case, the amplitudes of the subharmonic frequencies and the second harmonic decrease as the load increases, which may be due to the change in the system's stiffness or damping characteristics under higher loads, leading to a reduction in nonlinear vibration components.

Fig. 14 depicts the Y direction responses of disk 1 under a yawing maneuver (G = 2), comparing scenarios with and without rub-impact. As shown in Fig. 14a, the system's motion transitions between single-periodic, multi-periodic, and quasi-periodic states within the speed range of 500 rad/s to 1200 rad/s. This is followed by a predominantly quasi-periodic regime that spans from 1200 rad/s to 2100 rad/s, where the system exhibits sustained complex motion. A subsequent transition to single-periodic motion occurs at higher speeds, before a final shift back to quasi-periodic motion at 2450 rad/s. Conversely, the dynamics in Fig. 14b are characterized by a transition from quasi-periodic to single-periodic motion at low speeds (500 rad/s to 1450 rad/s). A quasi-periodic regime is observed between 1500 rad/s and 1900 rad/s, after which multi-periodic motion dominates until 2300 rad/s. Finally, the system settles into a persistent quasi-periodic motion from 2300 rad/s to 3000 rad/s.

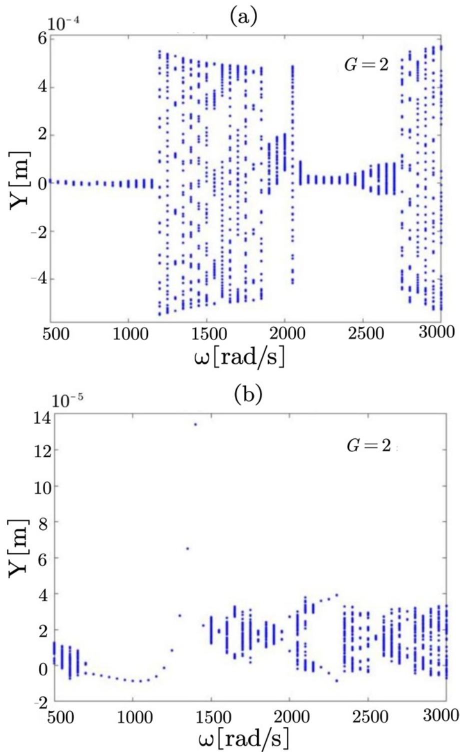

Fig. 14. Bifurcation diagram of disk 1 in the Y direction under yawing conditions (G = 2); a) rub-impact; b) no rub-impact

3.4 Pitching, Rolling and Yawing Maneuver Condition (Only Rub-Impact)

Figure 15 depicts the shaft orbits of three maneuvering loads in the disk 1 system under varying loads and rub factors. With increasing load, the amplitude of the yawing attitude in the X direction exhibits a more pronounced influence compared to those of the pitching and rolling attitudes. As the load increases, the displacement in the Y direction under pitching continues to grow, surpassing that of both yawing and rolling at G=5. Furthermore, a comparative analysis reveals that under lower load conditions (G=2.5), the rolling attitude contributes significantly to the vibration amplitudes in both the X and

Y directions. However, with further increase in load, its influence is exceeded by those of the yawing and pitching motions.

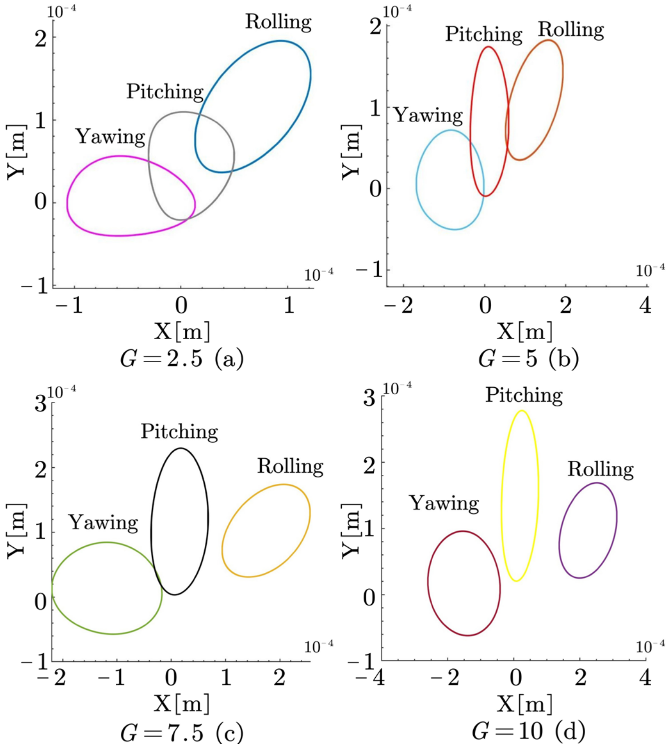

Fig. 15. **Shaft orbit diagrams of disk 1 under different flight postures under different maneuvering loads; a) G = 2.5, b) G = 5, c) G = 7.5, and d) G = 10**

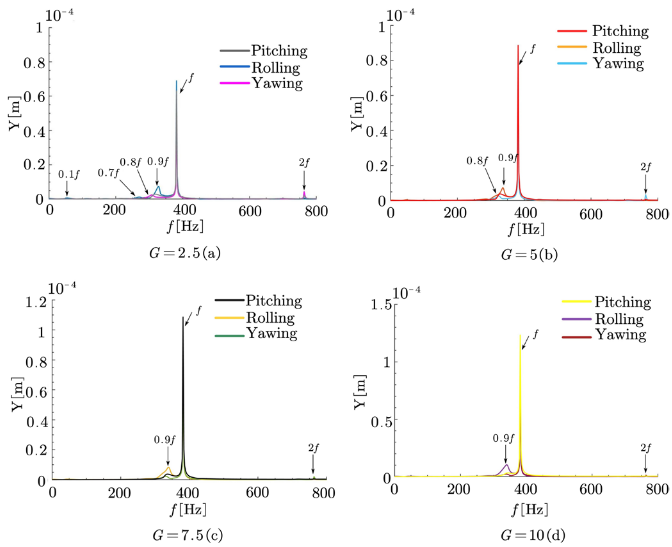

Fig. 16. Spectrogram (Y direction) of disk 1 in different flight postures under different maneuvering loads; a) G = 2.5, b) G = 5, c) G = 7.5, d) G = 10

The spectrum diagram of the Y direction for the disk 1 system under three different flight modes and various maneuvering loads, with rub-impact considered, is presented in Fig. 16. Based on the comparison, the pitching attitude produces the highest ($1f$) amplitude under all four loads. The rolling attitude consistently generates larger ($0.9f$) subharmonic amplitudes than the other attitudes, suggesting that rolling-induced rub-impact has a unique effect on the generation of this subharmonic component. In contrast, the yawing attitude yields the strongest components of the second harmonic ($2f$), highlighting that yawing maneuvers favor the generation of higher harmonic components under rub-impact

Under the coupling of fixed load G=2 and three flight attitudes (pitching, rolling, and yawing) with increasing speed, the disk 1 system's bifurcation diagram (Y direction) is displayed in Fig. 17. First, the three flying circumstances exhibit single-, multi-, and quasi-periodic motion, as well as comparatively rich periodic motion characteristics, and all of them exhibit strong nonlinear characteristics. And then, the most frequent alternation between periodic regimes is observed under pitching conditions.

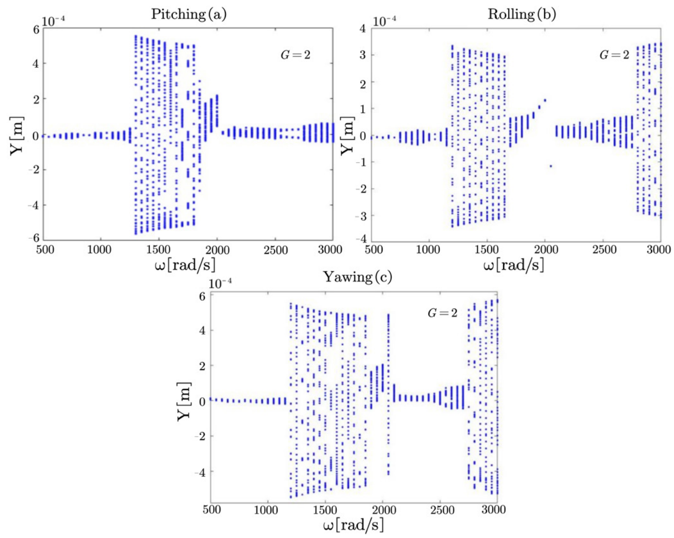

Fig. 17. **Bifurcation diagram of disk 1 maneuvering loads in Y direction; at a) pitching, b) rolling, and c) yawing conditions**

4 CONCLUSION

This study conducts a comprehensive comparative analysis of the dynamic behavior of an aero-engine dual-rotor system under three typical flight attitudes (pitching, rolling, and yawing) with different maneuver loads. The dynamic characteristics of the rub-impact versus the normal condition are examined under three different flight modes and various loads. Furthermore, the dynamic behavior among the three flight modes under dual-disk rubbing conditions is compared. Several notable phenomena with significant theoretical and practical implications are revealed, providing valuable insights for the design, vibration control, and failure analysis of fighter engine rotor systems.

1. According to the comparison, regardless of flight modes and related maneuvering load circumstances, vibration amplitudes in both the X and Y directions in orbit diagrams under dual-disk rub-impact faults constantly surpass those under non-rub conditions. Furthermore, spectrum graphs show much more varied frequency components during dual-disk rub-impact occurrences. Additionally, the bifurcation diagrams demonstrate that as the rotational speed increases, the vibration amplitudes under dual-disk rub-impact faults remain significantly higher than those under non-rub conditions across all flight modes and fixed loads. This indicates that the rub-impact not only amplifies vibration amplitudes but also sustains this amplification over a wide range of rotational speeds, posing a persistent threat to engine safety.
2. Under the coupled conditions of varying flight attitudes and dual-disk rub-impact faults, orbit diagrams show that pitching maneuvers (G=2.5, G=5 and G=7.5) have systematically higher vibration amplitudes in the Y direction than other flight attitudes, whereas yawing maneuvers have superior vibration amplitudes in the X direction. Across all three flight attitudes, the spectrograms under the G=2.5 condition exhibit more types of frequency com-

ponents with significant amplitudes compared to other maneuver loads, indicating that moderate maneuver loads create an optimal environment for the generation of complex nonlinear frequency components under the rub-impact. Furthermore, bifurcation diagrams show that the most frequent alternation between periodic regimes is observed under pitching conditions (G = 2 with rub-impact).

References

[1] Liang, C., Suo, D., Sun, M. A review on the key technologies of the sixth generation fighter engines in the us. *Aeroengine* 42 93-97 (2016).

[2] Sakata, M., Kimura, K., Park, S., Ohnabe, H. Vibration of bladed flexible rotor due to gyroscopic moment. *J Sound Vib* 131 (1989) 417-430 **DOI:10.1016/0022-460X(89)91002-X**.

[3] Sakata, M., Kimura, K., Okamoto, S., Oikawa, K. Vibration analysis of a high speed and light weight rotor system subjected to a pitching or turning motion: I: A rigid rotor system on flexible suspensions. *J Sound Vib* 184871-184885 (1995) **DOI:10.1006/jsvi.1995.0350**.

[4] Wei, H., Fan, X. Vibration response analysis of two-rotor systems in maneuvering flight. *Proc Conf Aeroengine Struct Strength Vib Chin Soc Aeronaut* 315-320 (2001).

[5] Zhu, C., Chen, Y. General dynamic model of aeroengine's rotor system during maneuvering flight. *J Aerosp Power* 24 371-377 (2009). (in Chinese)

[6] Hou, L., Chen, Y. Dynamical simulation and load control of a Jeffcott rotor system in Herbst maneuvering flight. *J Vib Control* 22 412-425 (2016) **DOI:10.1177/1077546314533138**.

[7] Han, Q., Chu, F. Dynamic response of cracked rotor-bearing system under time-dependent base movements. *J Sound Vib* 332 6847-6870 (2013) **DOI:10.1016/j.jsv.2013.07.025**.

[8] Chen, L., Wang, J., Han, Q., Chu, F. Nonlinear dynamic modeling of a simple flexible rotor system subjected to time-variable base motions. *J Sound Vib* 404 58-83 (2017) **DOI:10.1016/j.jsv.2017.05.032**.

[9] Kun, G., Xiuli, S., Yuanyuan, X., Haitao, L., Zhang, H. Initial research on impacts of maneuver loads on core engine tip clearance. *J Aerosp Power* 33 (2018) 2205-2218. (in Chinese)

[10] Pan, W., Ling, L., Qu, H., Wang, M. Coupling dynamic behavior of aero-engine rotor system caused by rolling, pitching and yawing maneuver loads. *Appl Math Model* 102 726-747 (2022) **DOI:10.1016/j.apm.2021.10.021**.

[11] Saeed, N.A., Awwad, E.M., Maarouf, A., Farh, H.M.H., Alturki, F.A., Awrejcewicz, J. Rub-impact force induces periodic, quasiperiodic, and chaotic motions of a controlled asymmetric rotor system. *Shock Vib* 2021 1800022 (2021) **DOI:10.1155/2021/1800022**.

[12] Wu, Z., Hao, L., Zhao, W., Ma, Y., Bai, S., Zhao, Q. Modeling and vibration analysis of an aero-engine dual-rotor-support-casing system with inter-shaft rub-impact. *Int J Non-Linear Mech* 165 104757 (2024) **DOI:10.2139/ssrn.4775226**.

[13] Prabith, K., Krishna, I.P. The stability analysis of a two-spool rotor system undergoing rub-impact. *Nonlinear Dyn* 104 941-969 (2021) **DOI:10.1007/s11071-021-06370-x**.

[14] Pan, W., Li, X., Ling, L., Qu, H. Dynamic modeling and response analysis of rub-impact rotor system with squeeze film damper under maneuvering load. *Appl Math Model* 114 544-582 (2023) **DOI:10.1016/j.apm.2022.10.021**.

[15] Lin, J., Wu, B., Lu, X., Xu, J., Zhang, J., Dai, H. Numerical simulation of aero-engine rotor-blade-coating coupling system with rub-impact fault and its dynamic response. *Proc Int Conf Rotor Dyn* 56-75 (2023) **DOI:10.1007/978-3-031-40459-7_4**.

[16] Sousa, M.S., Cavallini, A.A., Steffen, V., Briend, Y., Chatelet, E., Dufour, R. Numerical and experimental investigation of rubbing existence in the context of a rotating machine under base excitation. *J Vib Acoust* 147 041001 (2025) **DOI:10.1115/1.4068108**.

[17] Yu, P., Chen, G., Li, L. Modal analysis strategy and nonlinear dynamic characteristics of complicated aero-engine dual-rotor system with rub-impact. *Chin J Aeronaut* 35 184-203 (2022) **DOI:10.1115/1.4068108**.

[18] Yu, P., Guo, C., Cun, W., Mohan, Y. Modal characteristics and calculation method for flexible rotor system with rubbing constraint. *Acta Aeronaut Astronaut Sin* 41 224029-224029 (2020) **DOI:10.1016/j.cja.2020.10.031**.

[19] Fei, Z. R*esearch on finite element modeling and dynamic behaviors of complex multi-rotor coupled systems*, PhD Thesis. J Zhejiang Uni, Zhejiang (2013).

[20] Cheng, M., Meng, G., Wu, B. Nonlinear dynamics of a rotor-ball bearing system with Alford force. *J Vib Control* 18 17-27 (2012) **DOI:10.1177/1077546311405701**.

[21] Zhang, X., Yang, Y., Ma, H., Shi, M., Wang, P. A novel diagnosis indicator for rub-impact of rotor system via energy method. *Mech Syst Signal Process* 185 109825 (2023) **DOI:10.1016/j.ymssp.2022.109825**.

Received: 2025-06-09, revised: 2025-08-26, accepted: 2025-10-01 *as Original Scientific Paper.*

Data availability *The data supporting the study's findings are included in the paper.*

Author contribution *Peixun Tang: Data curation, Writing – original draft, Writing – review & editing; Peixun Tang: Formal analysis; Xiaojing Ma: Formal analysis; Xi Liu: Formal analysis; Peixun Tang: Validation; Zhengminqing Li: Validation.*

Dinamika dvorotorskih sistemov letalskih motorjev pri različnih letalnih položajih in sočasnih torno-udarnih stikih

Povzetek *Letala z visoko okretnostjo povzročajo izjemne obremenitve letalskih motorjev, kar lahko sproži uničujoče trke med rotorjem in statorjem ter tako predstavlja resno grožnjo varnosti leta. V tej študiji je bil vzpostavljen model rotorja z ležaji in diski s štirimi prostostnimi stopnjami za sistem z dvema diskoma, posebej zasnovan za simulacijo sklopljenih učinkov sočasnih trkov med rotorjem in statorjem obremenitvah v manevrih. Za primerjavo je bil izdelan tudi referenčni model brez trkov. Rešitve za oba modela so bile pridobljene z metodo Newmark-β. Za oceno vpliva manevrskih obremenitev na dinamične značilnosti sistema je bila izvedena parametrična analiza učinkov hkratnih trkov obeh diskov pri treh ključnih letalnih načinih – valjanju (rolling), nagibanju (pitching) in smernem zasuku (yawing). Raziskava ponuja pomembno teoretično osnovo za izboljšanje nadzora vibracij in izvedbo analiz odpovedi pri zasnovi motorjev bojnih letal ter tako prispeva k razvoju varnejših in zanesljivejših rotorskih sistemov.*

Ključne besede *dinamika rotorja, manevrski let, nelinearna ležajna sila, torno-udarni stik, nelinearne karakteristike*